



Article

Enhancing Lithium and Sodium Storage Properties of TiO₂(B) Nanobelts by Doping with Nickel and Zinc

Denis P. Opra ^{*}, Sergey V. Gnedenkov , Sergey L. Sinebryukhov , Andrey V. Gerasimenko, Albert M. Ziatdinov, Alexander A. Sokolov, Anatoly B. Podgorbunsky, Alexander Yu. Ustinov, Valery G. Kuryavyi, Vitaly Yu. Mayorov, Ivan A. Tkachenko and Valentin I. Sergienko

Institute of Chemistry, Far Eastern Branch of the Russian Academy of Sciences, 690022 Vladivostok, Russia; svy21@hotmail.com (S.V.G.); sls@ich.dvo.ru (S.L.S.); gerasimenko@ich.dvo.ru (A.V.G.); ziatdinov@ich.dvo.ru (A.M.Z.); alexsokol90@mail.ru (A.A.S.); pab@ich.dvo.ru (A.B.P.); all_vl@mail.ru (A.Y.U.); kvg@ich.dvo.ru (V.G.K.); 024205@inbox.ru (V.Y.M.); tkachenko@ich.dvo.ru (I.A.T.); sergienkovi@yandex.ru (V.I.S.)

^{*} Correspondence: dp.opra@ich.dvo.ru; Tel.: +7-(423)-2311889



Citation: Opra, D.P.; Gnedenkov, S.V.; Sinebryukhov, S.L.; Gerasimenko, A.V.; Ziatdinov, A.M.; Sokolov, A.A.; Podgorbunsky, A.B.; Ustinov, A.Y.; Kuryavyi, V.G.; Mayorov, V.Y.; et al. Enhancing Lithium and Sodium Storage Properties of TiO₂(B) Nanobelts by Doping with Nickel and Zinc. *Nanomaterials* **2021**, *11*, 1703. <https://doi.org/10.3390/nano11071703>

Academic Editor:
Christophe Detavernier

Received: 8 June 2021
Accepted: 24 June 2021
Published: 28 June 2021

Publisher's Note: MDPI stays neutral with regard to jurisdictional claims in published maps and institutional affiliations.



Copyright: © 2021 by the authors. Licensee MDPI, Basel, Switzerland. This article is an open access article distributed under the terms and conditions of the Creative Commons Attribution (CC BY) license (<https://creativecommons.org/licenses/by/4.0/>).

Abstract: Nickel- and zinc-doped TiO₂(B) nanobelts were synthesized using a hydrothermal technique. It was found that the incorporation of 5 at.% Ni into bronze TiO₂ expanded the unit cell by 4%. Furthermore, Ni dopant induced the 3d energy levels within TiO₂(B) band structure and oxygen defects, narrowing the band gap from 3.28 eV (undoped) to 2.70 eV. Oppositely, Zn entered restrictively into TiO₂(B), but nonetheless, improves its electronic properties (E_g is narrowed to 3.21 eV). The conductivity of nickel- ($2.24 \times 10^{-8} \text{ S}\cdot\text{cm}^{-1}$) and zinc-containing ($3.29 \times 10^{-9} \text{ S}\cdot\text{cm}^{-1}$) TiO₂(B) exceeds that of unmodified TiO₂(B) ($1.05 \times 10^{-10} \text{ S}\cdot\text{cm}^{-1}$). When tested for electrochemical storage, nickel-doped mesoporous TiO₂(B) nanobelts exhibited improved electrochemical performance. For lithium batteries, a reversible capacity of 173 mAh·g⁻¹ was reached after 100 cycles at the current load of 50 mA·g⁻¹, whereas, for unmodified and Zn-doped samples, around 140 and 151 mAh·g⁻¹ was obtained. Moreover, Ni doping enhanced the rate capability of TiO₂(B) nanobelts (104 mAh·g⁻¹ at a current density of 1.8 A·g⁻¹). In terms of sodium storage, nickel-doped TiO₂(B) nanobelts exhibited improved cycling with a stabilized reversible capacity of 97 mAh·g⁻¹ over 50 cycles at the current load of 35 mA·g⁻¹.

Keywords: TiO₂(B); doping; nanobelts; mesoporosity; lithium-ion battery; sodium storage; anode; safety; electrochemical performance

1. Introduction

Up until recently, electrochemical energy storage devices, among which lithium-ion batteries (LIBs) are dominant, were mainly used for areas that demanded moderate characteristics and soft operating standards (e.g., portable electronics, medical equipment, and power tools). At present, they are closely considered for usage in hybrid and electric vehicles, renewable energy, robotics, and standby backup power applications. However, due to the fundamental physicochemical properties of carbonaceous anode-active material (the voltage of Li⁺ insertion is close to that of Li metal formation, thereby causing its dendritic deposition; this is critical for charge in high-rate or low-temperature conditions), LIBs suffers restricted performance for such aims, especially in terms of charging rate, operating temperature range, and safety [1–3]. To avoid these problems, a negative electrode based on lithium pentatitanate with an operating potential of 1.55 V vs. Li/Li⁺ [4] was recently proposed and successfully commercialized (for example, in Mitsubishi i-MiEV and Honda Fit EV electric cars). Another important advantage of Li₄Ti₅O₁₂ is cycle life upon lithiation/delithiation due to its so-called “zero-strain” property. At the same time, the specific capacity of Li₄Ti₅O₁₂ is limited to 175 mAh·g⁻¹ [5]; hence, designing other materials, in which more Li can be accumulated, is needed to achieve further progress in terms of the charge rate and temperature range of LIBs. One such material can be titanium

dioxide, which possesses an Li-storage capacity of up to $335 \text{ mAh}\cdot\text{g}^{-1}$ [6] at a similar Li^+ insertion voltage of 1.5–1.8 V vs. Li/Li^+ (depending on the crystal structure). In this way, layered structural monoclinic (space group $C2/m$) bronze titanium dioxide ($\text{TiO}_2(\text{B})$) showed the most favorable performance as an LIB anode in comparison with other natural polymorphs [7,8]. The $\text{TiO}_2(\text{B})$ framework belongs to ReO_3 -type structure [9,10], which is presented by packings of ReO_3 blocks composed of distorted TiO_6 octahedra sharing the corners. The linking of blocks in the [001] direction is achieved through common edges. The packing of ReO_3 blocks in the [010] direction is displaced to a neighboring one by $a/2$ (a is unit cell parameter) along the [100] direction. Therefore, $\text{TiO}_2(\text{B})$ has an open structure with infinite channels running parallel to the b -axis. Such structural features govern the lithium insertion into bronze TiO_2 as a pseudocapacitive faradaic process [11], which is not hampered by sluggish solid-state diffusion unlike anatase, rutile, or brookite. Moreover, $\text{TiO}_2(\text{B})$ has a lower Li^+ insertion potential (near 1.5 V) compared to other natural polymorphs, resulting in higher energy density of the battery.

On the other hand, lithium reserves in the Earth's crust are limited, and the cost of lithium-containing raw materials is growing steadily. In this way, a change to other electrochemical energy storage technologies based on abundant materials, such as sodium-ion batteries (SIBs), is expected in the near future, at least for renewable energy and uninterruptible power supply fields [12,13]. At the same time, due to the unsuitability of graphite, other materials are being studied intensively as an anode for SIBs [14,15]. In view of the background and progress regarding LIBs over the past three decades, it may be postulated that intercalation-type materials are the most valuable for these purposes. However, as known, one of the main differences between SIBs and LIBs is the radius of charge carrier (1.02 Å for Na^+ and 0.76 Å for Li^+), which ensure an electrochemical process. Therefore, the search for materials with acceptable stability of structure (preferably with layered or tunnel crystal frameworks) under cyclic Na^+ insertion and extraction is an urgent task. Furthermore, the near-zero potential vs. Na/Na^+ of a hypothetical anode material may result in metallic sodium deposition on its surface, which limits battery operation and causes safety problems. Due to these reasons, titanium compounds based on the $\text{Ti}^{3+}/\text{Ti}^{4+}$ redox couple, including NaTiO_2 , $\text{Na}_2\text{Ti}_3\text{O}_7$, TiO_2 , $\text{Na}_2\text{Ti}_6\text{O}_{13}$, $\text{Na}_2\text{Ti}_4\text{O}_9$, $\text{NaTi}_2(\text{PO}_4)_3$, and ATiOPO_4 ($A = \text{NH}_4, \text{K}, \text{Na}$), have attracted attention [16,17]. Regarding four common TiO_2 polymorphs, it was found that bronze titanium dioxide possesses the best sodium storage properties [18,19]. The potential of $\text{TiO}_2(\text{B})$ vs. Na/Na^+ is 0.6–0.9 V [20], making it suitable as an SIB anode in terms of both energy density and safety concerns.

Unfortunately, $\text{TiO}_2(\text{B})$ is a wide-band gap semiconductor (its calculated band gap energy ranges between 3.09 and 3.22 eV [11,21]) with low electrical conductivity ($\sim 10^{-12} \text{ S}\cdot\text{cm}^{-1}$). In addition, the cyclic performance of $\text{TiO}_2(\text{B})$, depending on its volume variations upon the insertion and extraction of guest ions, especially in the case of accommodating large Na^+ , needs to be improved.

Up to date, a number of strategies have been proposed to address these issues, such as morphology tailoring, fabrication of composites, and metal and/or nonmetal doping. It has been revealed that success necessitates a combination of approaches involving microstructure tuning and doping routes. Indeed, when $\text{TiO}_2(\text{B})$ is reduced to nanoscale, e.g., nanotubes [22,23], nanorods [24], nanofibers [25], nanoribbons [26], nanowires [27,28], or nanoplates [29], it usually shows enhancing rate properties as an anode. Moreover, special attention should be paid to the mesoporosity of nanomaterials, which effectively ensures electrolyte penetration and charge carrier transport. On the other hand, doping titanium dioxide with metals/nonmetals [30–33] further increases its electrical conductivity due to the formation of local energy states inside the band structure and/or the generation of lattice defects (oxygen vacancies, Ti^{3+} species). Furthermore, controlling the variation in the radius of host and doped ions [34,35], as well as supporting the oxygen deficiency [36], may provide an increased stability and activity of $\text{TiO}_2(\text{B})$ during cycling in SIBs.

Herein, we successfully synthesized mesoporous $\text{TiO}_2(\text{B})$ nanobelts doped with nickel and zinc through a hydrothermal reaction. It is expected that, in terms of lithium and

sodium battery performance, Ni and Zn may be suitable dopants for TiO₂(B), providing both enhanced cyclability and rate capability. As suggested, the main factors determining such improved electrochemical behavior of doped TiO₂(B) are (i) increased conductivity of the material, (ii) improved stability of its structure during insertion/extraction of guest ions, and (iii) facilitated diffusion of charge carriers.

2. Materials and Methods

2.1. Synthetic Procedure

For preparing mesoporous nanobelts of doped TiO₂(B), anatase with an average particle size of ~100 nm (Alfa Aesar, Ward Hill, MA, USA), nickel and zinc nitrate hexahydrates (Merck, Darmstadt, Germany) and aqueous solutions of sodium hydroxide (14 M) and hydrochloric acid (0.05 M) were used as precursors. In brief, 0.1 g of anatase was dispersed in 15 mL of 14 M NaOH under vigorous stirring on a magnetic stirrer for 20 min. Then, a weighed portion of Ni(NO₃)₂·6H₂O or Zn(NO₃)₂·6H₂O was added in the solution in order to obtain the following atomic ratios of doped metal to titanium: 0.02, 0.05, and 0.08. The resultant solution was transferred to a 20 mL Teflon-lined stainless-steel autoclave and heated at 170 °C for 72 h. After the reaction, the product was cooled naturally to room temperature, separated on a 5804R centrifuge (Eppendorf, Hamburg, Germany), rinsed in 0.05 M HCl (three times, 75 mL each) for Na⁺/H⁺ exchange, washed in deionized water until the pH became neutral, and dried in air at 80 °C. Finally, the sample was treated thermally under vacuum (1 Pa) at 450 °C for 3 h to crystallize the bronze phase. The obtained series of materials were designated as TO-Ni-z and TO-Zn-z, where z represents the content of doped metal. The undoped TiO₂(B) (hereinafter TO) was fabricated using a similar procedure, but without Ni(NO₃)₂·6H₂O and Zn(NO₃)₂·6H₂O.

2.2. Characterization

Powder X-ray diffraction data (XRD) for samples were collected on a SmartLab from (Rigaku, Tokyo, Japan) and D8Advance (Bruker, Billerica, MA, USA) diffractometers using CuK_α-radiation (8048.0 eV). The crystalline phases were identified via a comparison of obtained patterns with PDF-2 (2015) cards. The lattice parameters were refined through Rietveld analysis using the JANA2006 program (ver. 25 June 2021) developed in the Institute of Physics of Academy of Sciences of the Czechia (Praha, Czechia). The morphology was studied by scanning (SEM) and scanning transmission (STEM) electron microscopy on a S5500 microscope from the Hitachi (Tokyo, Japan) equipped with a Duo-STEM detector. The elemental composition was investigated using an electron probe X-ray microanalyzer coupled to a S5500. The element distribution maps were obtained on a TM3000 microscope (Hitachi, Tokyo, Japan) with a Quantax 70 energy-dispersive X-ray spectrometer (EDX). Nitrogen adsorption/desorption isotherms were registered on an ASAP 2020 instrument (Micrometrics, Norcross, GA, USA) at 77 K. The specific surface area and pore size distribution were calculated using Brunauer–Emmett–Teller (BET) and Barrett–Joyner–Halenda (BJH) theories. The chemical state of elements was determined using X-ray photoelectron spectroscopy (XPS) on a SPECS system (SPECS, Berlin, Germany) equipped with a Phoibos-150 hemispherical energy analyzer using an MgK_α-source (1253.6 eV). The XPS binding energy scale was calibrated against the position of C 1s hydrocarbons (285.0 eV). The conductivity of samples was tested using the electrochemical impedance spectroscopy (EIS) technique at room temperature with a two-electrode cell on a SI1260 instrument from the Solartron Analytical (Farnborough, Hampshire, UK) over the frequency range 10⁻²–10⁶ Hz. For deeper insight into the electronic properties of materials, electronic paramagnetic resonance (EPR) and ultraviolet–visible spectroscopy (UV–Vis) analyses were performed. EPR spectra were recorded on an EMX6/1 spectrometer from the Bruker (Billerica, MA, USA) operating at X-band frequency with 100 kHz field modulation and a microwave power of 2.046 mW. UV–Vis spectra were obtained with a UV-2600 spectrophotometer (Shimadzu, Kyoto, Japan) equipped with an ISR-2600Plus integrating sphere. Barium sulfate was applied as a white reference. The magnetic properties were investigated on a

SQUID magnetometer MPMS (XL) from the Quantum Design (San Diego, CA, USA) in the temperature range of 2–300 K. The applied field dependence of magnetization was measured with steps of 100 and 500 Oe in the ranges from –2000 to 2000 Oe and from ± 2000 to $\pm 10,000$ Oe, respectively. The temperature dependence of magnetization was obtained under a magnetic field of 1000 Oe with a step of 2 K.

2.3. Electrochemical Measurements

The electrochemical parameters of TiO₂(B) nanobelts doped with nickel and zinc were tested using two-electrode ECC-STD cells from the El-Cell GmbH (Hamburg, Germany). The working electrodes were fabricated according to the standard doctor blade technique. In brief, active material, Timcal Super P carbon black, and polyvinylidene fluoride at a weight ratio of 80:13:7 (for LIBs) or 75:18:7 (for SIBs) were dispersed in *N*-methylpyrrolidone under protracted stirring to form a slurry. The binder was placed first, whereas active material and electroconductive additive were preliminary mixed using a Pulverisette 7 planetary mill (Fritch, Idar-Oberstein, Germany). Applying a MSK-AFA-I machine (MTI Corporation, Richmond, CA, USA), the slurry was casted uniformly on a copper foil current collector pretreated with diluted hydrochloric acid. After drying at 60 °C to constant weight, working electrodes were punched, pressed on a hydraulic press at 1000 kg·cm⁻², and heated under vacuum at 120 °C during 10 h. The active mass loading for individual electrodes was about 2 mg·cm⁻². Assembling electrochemical cells was carried out in an argon-filled glove box with moisture and oxygen below 5 ppm. A lithium or sodium metal foil was employed as the counter or reference electrode. The electrolyte for LIBs was 1 M LiPF₆ solution in a mixture of ethylene carbonate and diethyl carbonate at a volume ratio of 1:1 (Sigma-Aldrich, St. Louis, MO, USA). For SIBs, it was a 1 M solution of NaClO₄ in propylene carbonate with fluoroethylene carbonate additive (5 vol.%). A 2400 membrane from the Celgard (Charlotte, NC, USA) or GF/C glass fiber from the Whattman (Little Chalfont, Buckinghamshire, UK) was used as a separator for LIBs or SIBs, respectively. The cells were tested on a Celltest System (Solartron Analytical, Farnborough, Hampshire, UK) at room temperature in the potential range of 1–3 V (vs. Li/Li⁺) or 0.005–3 V (vs. Na/Na⁺). The performance parameters were measured by galvanostatic charge/discharge at various current densities from 30 to 1800 mA·g⁻¹. Cyclic voltammetry (CV) data were collected at a sweep rate of 0.1 mV·s⁻¹. The electrode impedance was measured from 10⁶ to 10⁻¹ Hz after five initial CV cycles (fully desodiated) following 6 h of rest to obtain the steady-state potential.

3. Results and Discussion

3.1. Structure, Morphology, and Electronic Properties of Ni- and Zn-Doped TiO₂(B) Nanobelts

XRD patterns of prepared materials are depicted in Figure 1. Their analysis revealed that monoclinic bronze of TiO₂ (PDF #46-1238, space group *C2/m*) was a dominant phase and tetragonal anatase (PDF #21-1272, space group *I41/amd*) was an impurity for all samples confirming the correct synthesis [37]. Furthermore, XRD data indicated traces of monoclinic anasovit (PDF #23-0606, space group *C2/m*) in the products obtained due to temperature-induced TiO₂(B)→Ti₃O₅ transitions [37]. No peaks of other phases were detected for TO-Ni-02, TO-Ni-05, and TO-Zn-02 samples. At the same time, NiO and ZnO were found in the compositions of TO-Ni-08 and TO-Zn-05, respectively, which were synthesized using high amounts of Ni(NO₃)₂·6H₂O and Zn(NO₃)₂·6H₂O precursors. Note that nickel oxide was formed only at the Ni/Ti ratio of 0.08, whereas zinc oxide was obtained already at Zn/Ti = 0.05. These data indicate that the solubility limit of dopant through the substitutional mechanism within titanium dioxide was reached. Hence, a further increase in dopant concentration would not be rational.

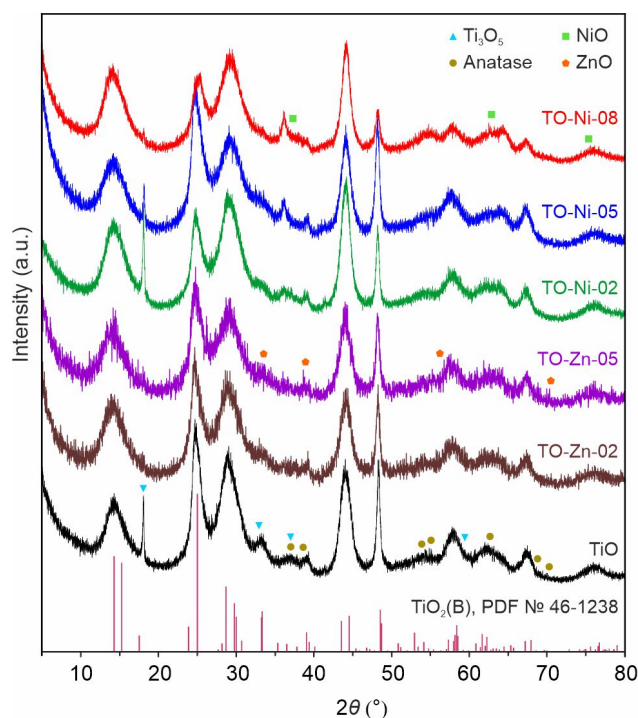


Figure 1. XRD patterns for as-synthesized samples doped with nickel and zinc $\text{TiO}_2(\text{B})$.

Through Rietveld refinement (Figure S1 and Table S1, Supplementary Materials), the lattice parameters for unmodified titanium dioxide were calculated as $a = 12.393(2) \text{ \AA}$, $b = 3.6863(9) \text{ \AA}$, $c = 6.505(1) \text{ \AA}$, and $\beta = 108.85(2)^\circ$. Doping with nickel changed these parameters, increasing the unit cell volume by 3–4%: from $281.23(9) \text{ \AA}^3$ for undoped $\text{TiO}_2(\text{B})$ to $289.0(1)$ and $291.8(1) \text{ \AA}^3$ for TO-Ni-02 and TO-Ni-05 samples, respectively. This was seemingly due to the larger radius of Ni^{2+} ions (0.69 \AA ; here and below, these values are given according to R.D. Shannon [38] for the coordination number of 6) occupying the Ti^{4+} sites (0.605 \AA). Upon a further increase in nickel content (TO-Ni-08), the volume of the unit cell decreased to $289.7(2) \text{ \AA}^3$, indicating a limitation in its incorporation into bronze TiO_2 crystal structure. From refined data, the lattice parameters of TO-Ni-05 were measured as $a = 12.269(4) \text{ \AA}$, $b = 3.795(1) \text{ \AA}$, $c = 6.601(2) \text{ \AA}$, and $\beta = 108.33(3)^\circ$. Similar to nickel, upon Zn doping, the lattice constants of $\text{TiO}_2(\text{B})$ were changed. Interestingly, the unit cell expanded by about 2% for the TO-Zn-02 product ($286.31(5) \text{ \AA}^3$). The large ionic radius of Zn^{2+} (0.74 \AA) probably hindered the accentuated occupation of Ti^{4+} positions. Analogous results were previously reported for Zn-doped anatase [39]. In this way, the absence of expected ZnO reflections in the XRD pattern of TO-Zn-02 could be explained by its low content.

The SEM images unveiled in Figure 2 demonstrate that synthesized materials had the same morphology and consisted of belt-like nanostructures. The dimensions of nanobelts were 40–160 nm in width, 3–7 nm in thickness and up to a few micrometers in length. It can be seen that Ni-doped $\text{TiO}_2(\text{B})$, i.e., the TO-Ni-05 sample, showed a better dispersion and uniformity of belts as compared to others.

According to the STEM study of the TO-Ni-05 product (Figure 3a), the surface of Ni-modified bronze TiO_2 nanobelts was rough and porous. It is believed that these features may be valuable in terms of the electrochemical performance of the material as an anode for metal-ion batteries.

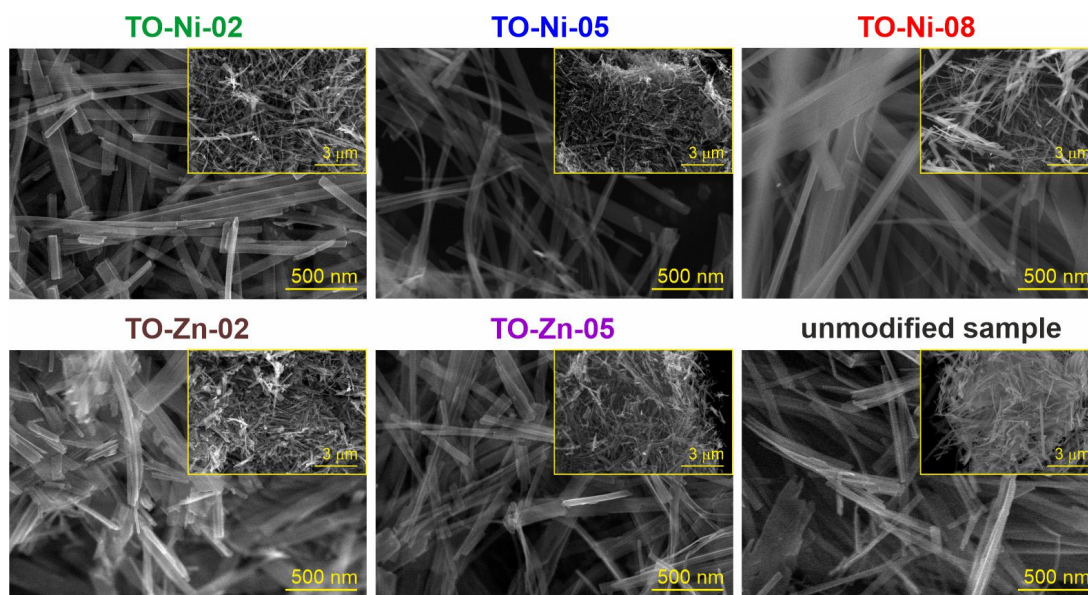


Figure 2. SEM images for titanium dioxide doped with nickel and zinc.

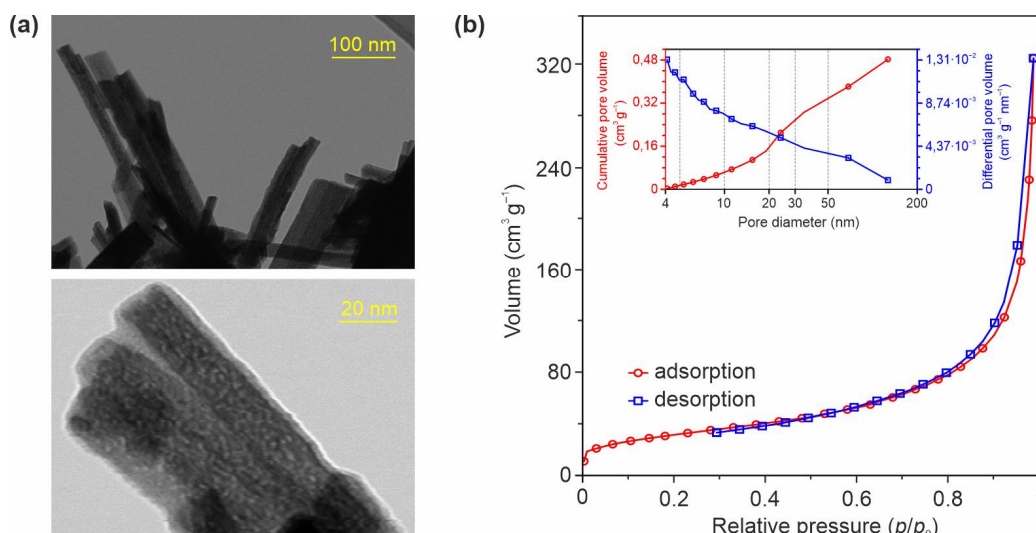


Figure 3. (a) Microphotographs in STEM mode at different magnification, (b) nitrogen adsorption/desorption isotherms at 77 K, and (inset) cumulative pore volume and pore size distribution curves for TO-Ni-05 material.

EDX microanalysis (Figure S2a, Supplementary Materials) confirmed that, along with Ti and O elements, the TO-Ni-05 product contained Ni. The Ti, O, and Ni distribution maps are depicted in Figure S2b (Supplementary Materials). The N_2 adsorption/desorption data (Figure 3b) show that the TO-Ni-05 material possessed a BET specific surface area of $114 \text{ m}^2 \cdot \text{g}^{-1}$ and a BJH pore volume of $0.48 \text{ cm}^3 \cdot \text{g}^{-1}$. The pore size distribution curve (Figure 3b, inset) of nickel-doped titanium dioxide with a maximum at $\sim 4.2 \text{ nm}$ shows that at least 70% of the pore volume was formed by mesopores. For the unmodified sample (Figure S3, Supplementary Materials) the BET surface area and BJH pore volume were lower: $40 \text{ m}^2 \cdot \text{g}^{-1}$ and $0.27 \text{ cm}^3 \cdot \text{g}^{-1}$. This means that doping had an effect on the texture of bronze TiO_2 nanobelts. According to the literature [40], the observed effect can be explained by the inhibition the growth of $\text{TiO}_2(\text{B})$ crystallites due to nickel staying at grain boundaries and the formation Ni–O–Ti bonds.

The chemical state of elements in Ni-doped $\text{TiO}_2(\text{B})$ nanobelts was investigated using the XPS method, as shown in Figure 4. According to analysis of the survey spectrum (Figure 4a), titanium, oxygen, and nickel elements existed in the TO-Ni-05 material. Fur-

thermore, carbon is detected in the sample due to adventitious contamination. The Ti 2*p* region in Figure 4b shows a doublet at 458.4 eV (Ti 2*p*_{3/2}) and 464.1 eV (Ti 2*p*_{1/2}). The splitting for Ti 2*p* was equal to 5.7 eV, meaning that titanium was in a +4 oxidation state [41]. The O 1*s* spectrum could be deconvoluted into two peaks, as shown in Figure 4c. The signal at 529.4 eV could be ascribed to oxygen chemically bound to titanium, while the peak at 530.7 eV was related to adsorbed water or organics [42]. Figure 4d illustrates the spectrum of Ni 2*p*_{3/2} centered at 854.0 eV, indicating that nickel was in the +2 state [43]. Through a quantitative XPS analysis of the surface composition for the TO-Ni-05 sample, the O/(Ti+Ni) atomic ratio was calculated to be close to 1.85 (Figure 4a, inset; excluding carbon contaminations). The oxygen deficiency in nickel-doped TiO₂(B) was probably due to neutralizing Ni²⁺ ions by oxygen vacancies in order to maintain the electrostatic balance [44], as defined in Equation (1).

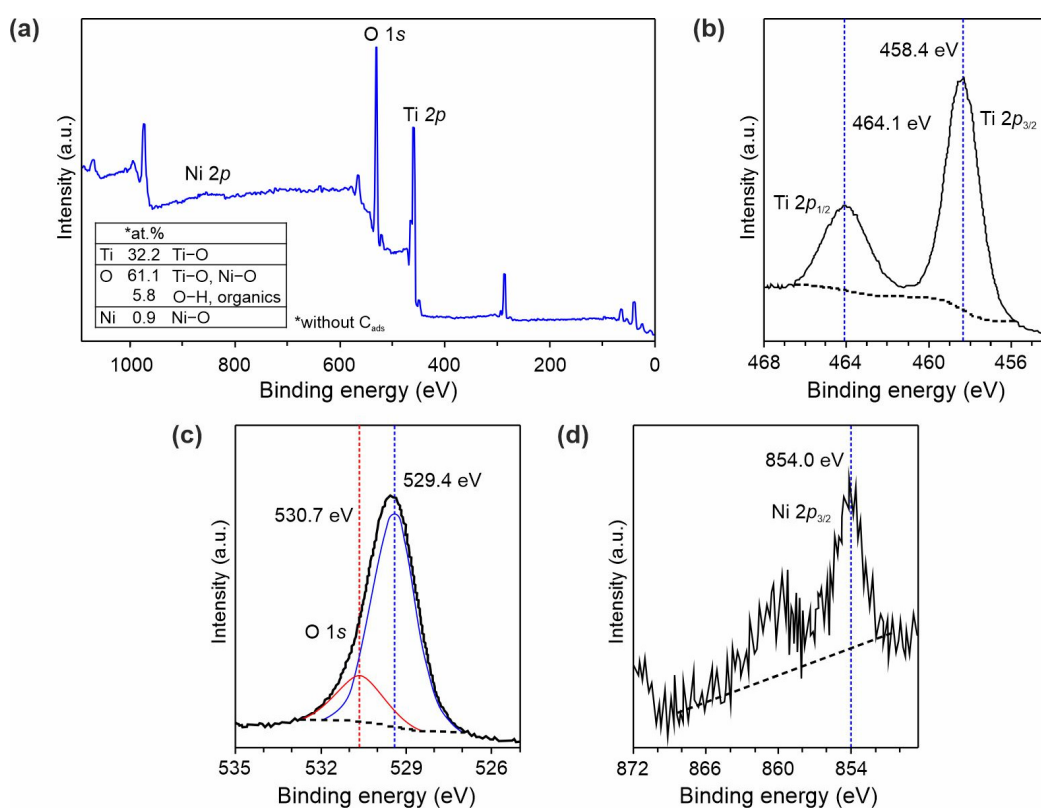


Figure 4. (a) XPS survey scan and high-resolution spectra of (b) Ti 2*p*, (c) O 1*s*, and (d) Ni 2*p* core levels for TO-Ni-05 sample.

In this way, it should be noted that recently reported density functional theory calculations [36] predicted lower sodiated energy barriers for oxygen-deficient bronze titanium dioxide, presuming greater activity of Na⁺ ions during insertion and extraction into/from the framework.

In order to study the effect of doping on TiO₂(B) electronic properties, EIS measurements were carried out for all samples. The representation of impedance spectra in Nyquist diagrams (*Z*'' vs. *Z*') reveals depressed semicircle, reflecting the conductivity of the material and arc characterizing the interfacial phenomena, as shown in the enlarged view in Figure 5a (full-scale range EIS spectra are given in Figure S4, Supplementary Materials). The analysis of impedance plots was performed in ZView 3.3c software using the electrical equivalent circuit (Figure 5a, inset), comprising the electrode resistance (*R*_{el}), bulk resistance of the sample (*R*_b) and its geometric capacitance (*C*_g), double-layer capacitance (*C*_{dl}), and charge transfer resistance (*R*_{ct}). According to impedance data fitting, the con-

ductivity of nickel-containing materials was calculated as $9.78 \times 10^{-10} \text{ S}\cdot\text{cm}^{-1}$ (TO-Ni-02), $2.24 \times 10^{-8} \text{ S}\cdot\text{cm}^{-1}$ (TO-Ni-05), and $5.48 \times 10^{-9} \text{ S}\cdot\text{cm}^{-1}$ (TO-Ni-08), whereas, for the TO sample, it was $1.05 \times 10^{-10} \text{ S}\cdot\text{cm}^{-1}$. Hence, the conductivity of titanium dioxide increased by approximately 100-fold after the incorporation of nickel dopant. In accordance with [45], this can be explained by the generation of a localized Ni 3d energy state within the TiO₂(B) band structure. It is important to note that the electronic properties of titanium dioxide were improved steadily up to Ni/Ti = 0.05, while a subsequent extension in nickel content (Ni/Ti = 0.08) was accompanied by a decrease in conductivity. This was seemingly due to low-to-moderate amounts of Ni²⁺ ions being successfully incorporated into the TiO₂(B) crystal lattice, while an excess of dopant led to the formation of an NiO phase with pronounced dielectric properties (conductivity equal to $10^{-13} \text{ S}\cdot\text{cm}^{-1}$ [46]). Regarding the TO-Zn-02 and TO-Zn-05 samples, it can be concluded that Zn doping also had an influence on the electroconductive properties of bronze TiO₂. In particular, the conductivity of TO-Zn-02 and TO-Zn-05 materials was measured as 3.29×10^{-9} and $2.09 \times 10^{-9} \text{ S}\cdot\text{cm}^{-1}$, respectively.

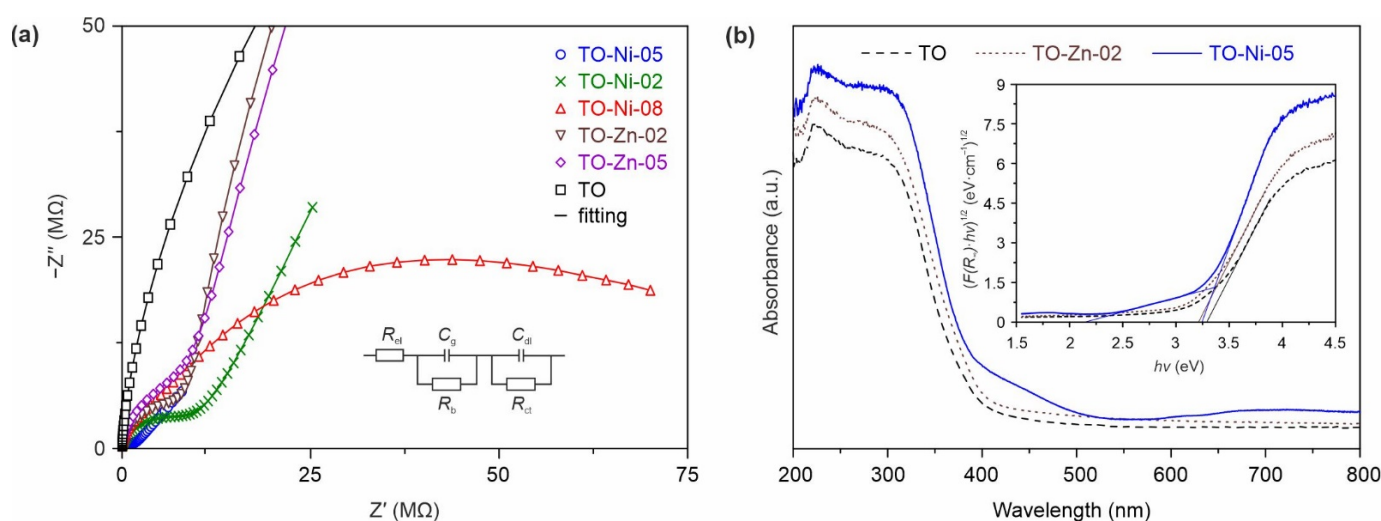


Figure 5. (a) EIS spectra (enlarged view) of TiO₂(B) materials containing different amounts of nickel and zinc and electrical equivalent circuit (inset) for fitting of the experimental impedance data. Symbols represent experiments, whereas lines are fitting results. (b) UV-Vis absorption data for TO, TO-Ni-05, and TO-Zn-02 products (inset represents corresponding Kubelka–Munk plots).

To gain insight into the electronic structure of nickel- and zinc-containing TiO₂(B), UV-Vis experiments were performed for TO, TO-Ni-05, and TO-Zn-02 materials in the wavelength range of 200–800 nm, as shown in Figure 5b. The data obviously reveal changes in the absorbance curve, with a shift in the absorption edge to the visible-light region for nickel-containing TiO₂(B) nanobelts. According to previous reports [45,47], this red shift may be related to the appearance of Ni 3d energy levels in the middle of the TiO₂ band gap. Furthermore, the spectrum of the TO-Ni-05 sample showed an absorption peak with a maximum at approximately 725 nm, the intensity of which strongly depended on nickel concentration (Figure S5, Supplementary Materials). This peak has previously been reported in the literature and was attributed to Ni²⁺ ions in the octahedral coordination [48]. With regard to Zn-doped TiO₂(B), its absorption edge also moved slightly toward longer wavelengths (i.e., red-shifted) as compared to the undoped sample. According to the literature [47], this may be due to the introduction of impure Zn 3d electronic levels mixed with the O 2p states. The band gap energy, E_g , of materials was estimated using the Tauc method (Equation (2)) for indirect ($\gamma = 2$) electron transition via the Kubelka–Munk function $F(R_\infty)$.

$$(F(R_\infty) \cdot h\nu)^{1/\gamma} = B(h\nu - E_g), \quad (2)$$

where $F(R_\infty) = (1 - R_\infty)^2 / 2R_\infty$ was used instead of the absorption coefficient α , $R_\infty = 10^{-4}$, A is the absorbance, h is the Planck constant, ν is the photon frequency, and B is a constant.

As revealed from measurements (Figure 5b, inset), doping with metals reduced the band gap of bronze titanium dioxide from 3.28 eV (TO) to 3.21 eV (TO-Zn-02) and 2.70 eV (TO-Ni-05).

Since EPR is an excellent technique for identifying the paramagnetic centers in materials, it was applied to study the Ni-doped TiO₂(B) nanobelts (Figure 6a). The EPR spectrum of TO-Ni-02 powder contained a high-intensity broad signal, a narrow component on its high-field shoulder, and a low-intensity asymmetric line with the *g*-factor equal to 4.35. The *g*-factor value is a characteristic of the ions in 3*d*⁵ electron configuration in the crystal fields with a strong rhombic component [49]. It was registered for all studied samples, including TO (Figure S6, Supplementary Materials), belonging to Fe³⁺ ions present in the precursor in trace amounts. Deconvolution of the TO-Ni-02 spectrum into components (designated as TO-Ni-02* in Figure 6a), excluding the contribution of the low-intensity signal of Fe³⁺, showed that the broad signal (N1) was characterized by *g* = 2.19, and the narrow one (N2) was characterized by *g* = 2.003. The *g*-factor value for component N1 is typical of Ni²⁺ ions in the octahedral crystal field [50,51]. Hence, it can be suggested that Ni²⁺ ions substituted the Ti⁴⁺ species in some octahedra within the TiO₂(B) lattice. Due to this Ni²⁺/Ti⁴⁺ replacement, the appearance of oxygen vacancies was required to maintain charge neutrality in the crystal structure [36,52]. The value of *g*-factor for component N2 is typical of so-called *F*-centers, i.e., electrons “trapped” by the structural defects. Accordingly, they may be the conduction band electrons “trapped” with the oxygen vacancies. The EPR spectrum of TO-Ni-05, without taking into account the contributions of low-intensity signals from Fe³⁺ and *F*-centers, can be represented as a superposition of two broad signals: the N1' component with *g* = 2.20 and the N3 contribution with *g* = 2.33 (TO-Ni-05* deconvolution in Figure 6a). As in the spectrum of the TO-Ni-02 material, the N1' component corresponded to Ni²⁺ ions embedded in the TiO₂(B) lattice at the Ti⁴⁺ positions. The N3 component, the *g*-factor value of which significantly exceeded that of isolated Ni²⁺ ions, possibly belonged to the ferromagnetically ordered structures of nickel, perhaps magnetic nickel clusters, formed from the excess dopant on its surface and/or in the pores [53]. In addition, the carrier of ferromagnetism in TO-Ni-05 can be an *F*-center-bound magnetic polaron [54,55]. In such a polaron, an electron trapped by an oxygen vacancy effectively binds the *d*-electrons of the surrounding magnetic ions. It is worth noting that, in the interpretation of the magnetic polaron model, the smaller intensity of the signal from *F*-centers in the sample synthesized with using a greater amount of nickel-containing precursor can be explained by the presence of the larger number of *F*-center-bound magnetic polarons in it.

Figure 6b represents the magnetic field dependence of magnetization under ambient conditions for the TO-Ni-05 product. The hysteresis loop for Ni-doped TiO₂(B) nanobelts was observed, showing ferromagnetism at room temperature. At the same time, it is known that pure titanium dioxide is diamagnetic. There is currently no unified explanation for the ferromagnetic properties arising in diamagnetic materials. Many researchers have explained this fact through the model of bound polarons [54,55]. However, there are an increasing number of studies suggesting that structural defects (oxygen vacancies) have a strong effect on the magnetic behavior of TiO₂ [55,56]. Accordingly, it seems that both mechanisms contributed to the ferromagnetism of Ni-containing TiO₂(B). Notably, the obtained hysteresis loop was asymmetric to the origin coordinates (Figure 6b, enlarged view of the *M*(*H*) curve), indicating the existence of antiferromagnetic/ferromagnetic interactions in the analyzed sample. The presence of an antiferromagnet phase was confirmed by the temperature dependence of magnetization (Figure 6b, inset of *M*(*T*) curve), in which the peak at a temperature of 68 K inherent to transition from an antiferromagnetic state was clearly observed. Nevertheless, we were unable to refer this temperature to the Néel temperatures of known antiferromagnets containing nickel and titanium. Moreover, it should be noted that defect regions with different spin orders can form on the surface of TiO₂ nanobelts, leading to strong exchange interactions of the antiferromagnet/ferromagnet type. Thus, to reveal the origin of shifting the hysteresis loop at a temperature of 300 K

and to identify the nature of antiferromagnetic phase in Ni-doped TiO₂(B) sample, an additional study is required.

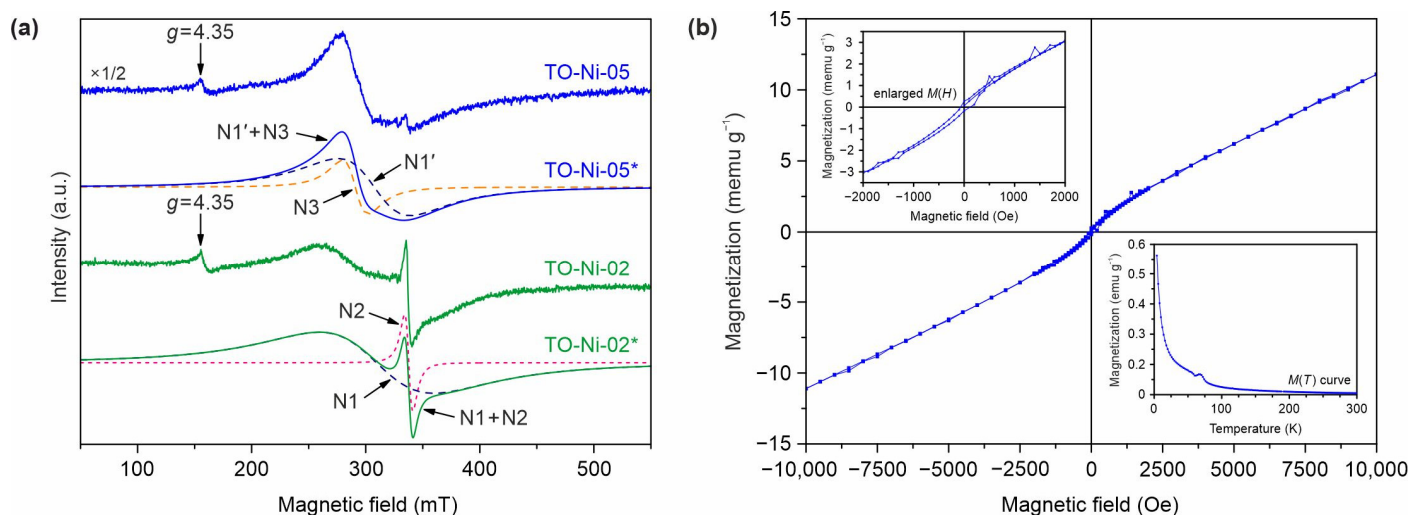
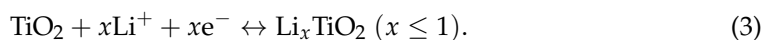


Figure 6. (a) Experimental and deconvoluted (marked by *) EPR spectra for TO-Ni-02 and TO-Ni-05 samples at 290 K. (b) Magnetic hysteresis loop at room temperature for TO-Ni-05 material. The insets show the enlarged view of the $M(H)$ curve in a low magnetic field and the temperature dependence of magnetization.

Thus, XRD, XPS, EIS, UV–Vis, EPR, and magnetization measurements confirmed the successful substitution of Ti atoms for Ni species in the TiO₂(B) structure, accompanied by the formation of solid solutions with general formula Ti_{1-x}Ni_xO_{2-δ}(B). The results are in a good accordance with the material morphology (Figure S7, Supplementary Materials). Indeed, the white color of unmodified bronze titanium dioxide became yellow after Ni doping. On the other hand, it was found that the zinc hardly entered into bronze TiO₂ lattice to substitute titanium, nevertheless enhancing its electronic properties. The color of the Zn-modified sample did not change after doping.

3.2. Electrochemical Performance of Ni- and Zn-Doped TiO₂(B) Nanobelts in Lithium and Sodium Batteries

Figure 7a represents the initial galvanostatic charge–discharge curves of the first cycle for TO-Ni-05, TO-Zn-02, and TiO electrodes registered in electrochemical half-cells against Li metal within the potential range of 1–3 V at the current density of 50 mA·g⁻¹. The profiles look similar for tested materials, showing an identical reaction mechanism associated with lithium ion intercalation/deintercalation into/from the titanium dioxide structure according to Equation (3).



The initial specific capacities of unmodified TiO₂(B) nanobelts were around 223 mAh·g⁻¹ (charge) and 165 mAh·g⁻¹ (discharge), showing a Coulombic efficiency of about 74%. The observed irreversibility during the first cycle (58 mAh·g⁻¹) may be explained by the presence of residuals on the surface (a further discussion is provided later) and the trapping of lithium ions into irreversible TiO₂ sites [57,58]. Furthermore, due to the presence of surface H₂O or O–H groups, nano-TiO₂-based anodes (as well as Li₄Ti₅O₁₂ [59]) may demonstrate certain reactivity toward the electrolyte, causing its decomposition during the first cycle through the formation of a solid electrolyte interphase layer (SEI) [60,61]. Doping with zinc decreased the initial losses to 49 mAh·g⁻¹. Indeed, during the first cycle, the TO-Zn-02 electrode gave 219 and 170 mAh·g⁻¹ upon lithiation and delithiation, respectively, revealing that over 77% of initial storage was maintained. This may have been due to ZnO decreasing the surface reactivity, thereby mitigating the electrolyte decomposition upon first lithium insertion [62]. Regarding the TO-Ni-05 sample, charging

and discharging capacities of 254 and 189 $\text{mAh}\cdot\text{g}^{-1}$ were registered. Thus, it can be suggested that Ni-doped bronze titanium dioxide revealed better lithium storage than unmodified and Zn-containing $\text{TiO}_2(\text{B})$. At the same time, the TO-Ni-05 electrode possessed the greatest irreversible losses during the first cycle ($65 \text{ mAh}\cdot\text{g}^{-1}$). This was seemingly due to its large specific surface area and high porosity.

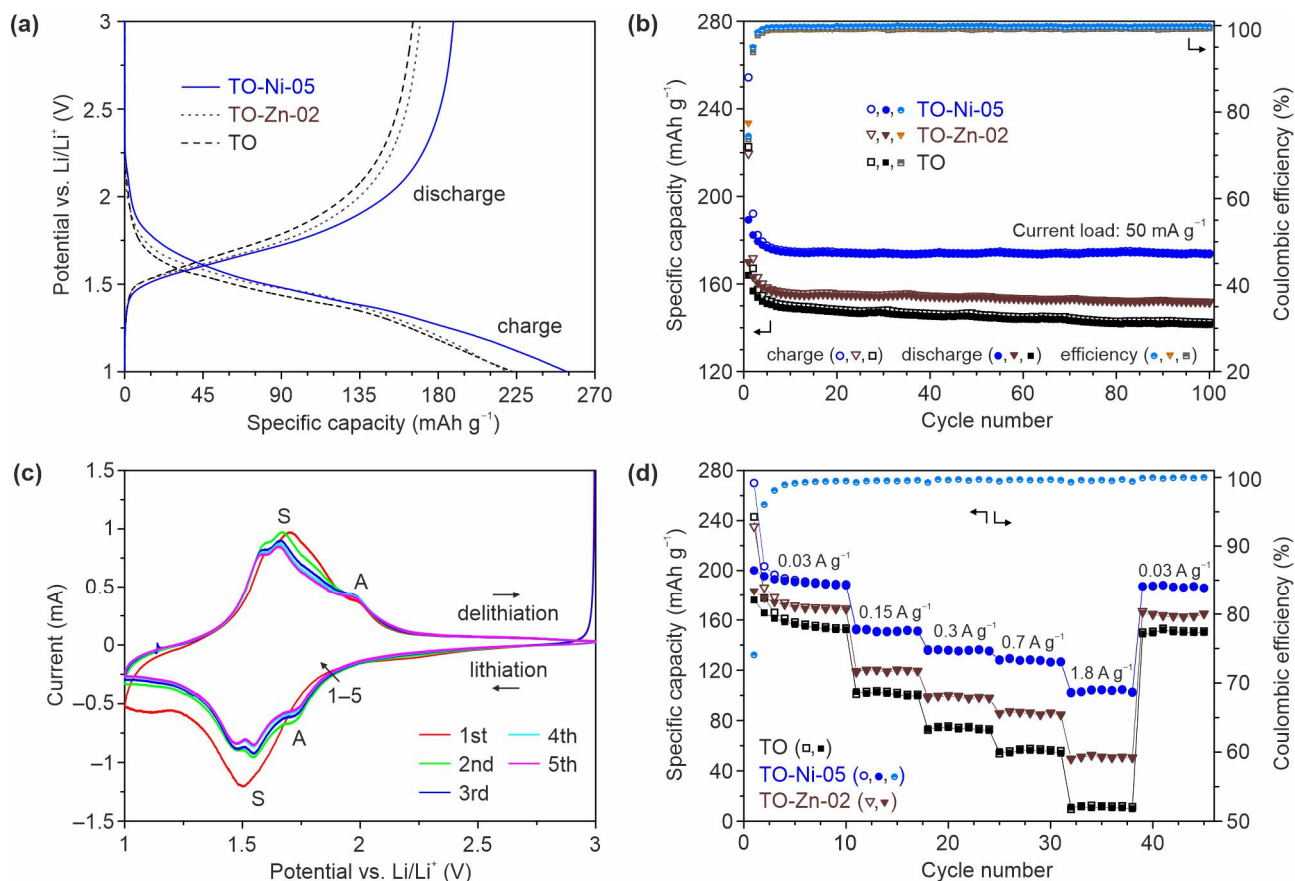


Figure 7. Lithium-ion battery performance of Ni- and Zn-doped bronze titanium dioxide. Charge/discharge curves of the first cycle (a) and cyclability (b) at the current load of $50 \text{ mA}\cdot\text{g}^{-1}$ for unmodified, Ni-doped, and Zn-doped $\text{TiO}_2(\text{B})$ materials. CV data for TO-Ni-05 at a scan rate of $0.1 \text{ mV}\cdot\text{s}^{-1}$ (c). Rate performances at different current densities of 30, 150, 300, 700, and 1800 $\text{mA}\cdot\text{g}^{-1}$ (d) for TO, TO-Ni-05, and TO-Zn-02 electrodes.

The detected positive effect from nickel doping became more evident during continuous testing of the materials, as shown in Figure 7b. The main capacity decay for analyzed samples occurred during the initial 6–7 cycles, after which the cycling performance stabilized. This continuing degradation was associated with the loss of guest Li^+ ions within the host TiO_2 lattice and SEI variations. During the 10th cycle, Ni-doped $\text{TiO}_2(\text{B})$ nanobelts kept around 92% of their initial reversible capacity. Upon further cycling, the average capacity decay for TO-Ni-05 was merely around $0.01 \text{ mAh}\cdot\text{g}^{-1}$ per cycle, which is an obvious improvement compared to TO ($\sim 0.08 \text{ mAh}\cdot\text{g}^{-1}$) and TO-Zn-02 ($\sim 0.04 \text{ mAh}\cdot\text{g}^{-1}$). The specific capacity of about $173 \text{ mAh}\cdot\text{g}^{-1}$ could be maintained after 100 cycles for Ni-containing $\text{TiO}_2(\text{B})$ nanobelts. In the case of undoped and Zn-modified materials, capacities of approximately 140 and $151 \text{ mAh}\cdot\text{g}^{-1}$, respectively, were achieved at the 100th cycle. Note that the results obtained for undoped $\text{TiO}_2(\text{B})$ nanobelts are in good accordance with the literature [63,64].

To analyze the electrochemical Li^+ -insertion/extraction behavior of Ni-doped $\text{TiO}_2(\text{B})$, CV tests (Figure 7c) were performed in the voltage range from 1 to 3 V at a scan rate of $0.1 \text{ mV}\cdot\text{s}^{-1}$. It can be seen that a few redox peaks existed in CV curves. A pair of intense peaks with precise splitting (so-called S-peaks [11]) at around 1.47/1.55 V (cathode region)

and 1.58/1.66 V (anode region) could be attributed to lithiation and delithiation of $\text{TiO}_2(\text{B})$, while the cathode and anode peaks near 1.72 and 1.98 V (A-peaks) were related to anatase. It is noteworthy that S-peaks in CVs almost completely overlapped in subsequent cycles, showing the good stability of the $\text{TiO}_2(\text{B})$ lattice containing Ni dopant. The broad cathode peak between 2.06 and 2.42 V registered in the first cycle had no pair in the corresponding anode region, as well as no overlap in subsequent CVs, indicating that the irreversible nature of this process caused its appearance. According to [57], it is associated with the presence of residual water or carbon species and radicals adsorbed on the surface of titanium dioxide nanoparticles (consistent with XPS data).

By testing rate performance (Figure 7d), a reversible capacity of around $101 \text{ mAh}\cdot\text{g}^{-1}$ was obtained for undoped bronze titanium dioxide nanobelts at the current load of $150 \text{ mA}\cdot\text{g}^{-1}$, which then decreased to about 73, 55, and $11 \text{ mAh}\cdot\text{g}^{-1}$ at current rates of 300, 700, and $1800 \text{ mA}\cdot\text{g}^{-1}$, respectively. It is known that, along with simplicity of preparation, belt-like $\text{TiO}_2(\text{B})$ nanostructures possess poorer rate characteristics (close to bulk $\text{TiO}_2(\text{B})$ [65,66]) as compared to others (Figure S8 and Table S2, Supplementary Materials). At the same time, when doped, bronze titanium dioxide nanobelts demonstrate an improved rate capability with higher delivered capacity. In particular, upon increasing the current density to 150, 300, 700, and $1800 \text{ mA}\cdot\text{g}^{-1}$, the TO-Zn-02 electrode maintained about 117, 95, 83, and $48 \text{ mAh}\cdot\text{g}^{-1}$. However, the best properties were detected for Ni-containing $\text{TiO}_2(\text{B})$, i.e., the TO-Ni-05 sample; a reversible specific capacity of approximately 152, 136, 128, and $104 \text{ mAh}\cdot\text{g}^{-1}$ was achieved at rates of 150, 300, 700, and $1800 \text{ mA}\cdot\text{g}^{-1}$, respectively. This was seemingly due to the enhanced textural characteristics and improved conductive properties of the TO-Ni-05 product. Thus, the direct comparison in terms of cycling and rate performance of bronze titanium dioxide nanomaterials tested in this work indicated an impressive effect of Ni dopant. Hence, it is believed that the reported results may be useful for preparing advanced $\text{TiO}_2(\text{B})$ -based anodes for LIBs using such effective nanostructures as nanofibers, nanowires, nanotubes, and nanosheets and/or for preparing hybrids and nanocomposites with carbonaceous materials (especially graphene). After high-rate testing, it was observed that TO-Ni-05 restored its capacity without obvious losses when the current load returned to $30 \text{ mA}\cdot\text{g}^{-1}$. It should be noted that, according to previous reports, the achieved rate capability results may be further enhanced through the optimization of electrode fabrication and rate test conditions, including carbon additive content and pressing options [57], type of applied binder or electrolyte composition [67], employed cutoff potentials (usually 1.2 and 2.5 V [68]), or charge procedure [69]. However, such experiments are outside the scope of this study and may be performed later.

The electrochemical performance of Ni-doped $\text{TiO}_2(\text{B})$ nanobelts was next tested in SIBs, contributing to the search for materials having an open structure with a tolerable lattice distortion upon continuous sodium ion insertion/extraction. Figure 8a depicts the five initial charge/discharge voltage profiles of the TO-Ni-05 electrode, registered between cutoff potentials of 0.005 and 3 V at a current density of $35 \text{ mA}\cdot\text{g}^{-1}$. The data show that sodiation and desodiation capacities of around 337 and $133 \text{ mAh}\cdot\text{g}^{-1}$ were ascertained for the TO-Ni-05 sample during the first cycle. Hence, the initial Coulombic efficiency for the material was calculated to be about 40%, indicating huge irreversible capacity losses ($204 \text{ mAh}\cdot\text{g}^{-1}$), in accordance with other TiO_2 -based anode materials for SIBs. According to a literature review [70–72], the main reasons for this observed irreversibility are (i) side reactions at the electrode/electrolyte interface (usually more intense for mesoporous materials with a relatively high specific surface area, such as TO-Ni-05), (ii) trapping of some Na^+ ions within the $\text{TiO}_2(\text{B})$ lattice, (iii) amorphization of anatase due to interactions with sodium, and (iv) sodiation of the comprised conductive carbon. Meanwhile, an analysis of subsequent voltage curves demonstrated that they almost overlapped after the third cycle, presenting good reversibility following the electrochemical storage process.

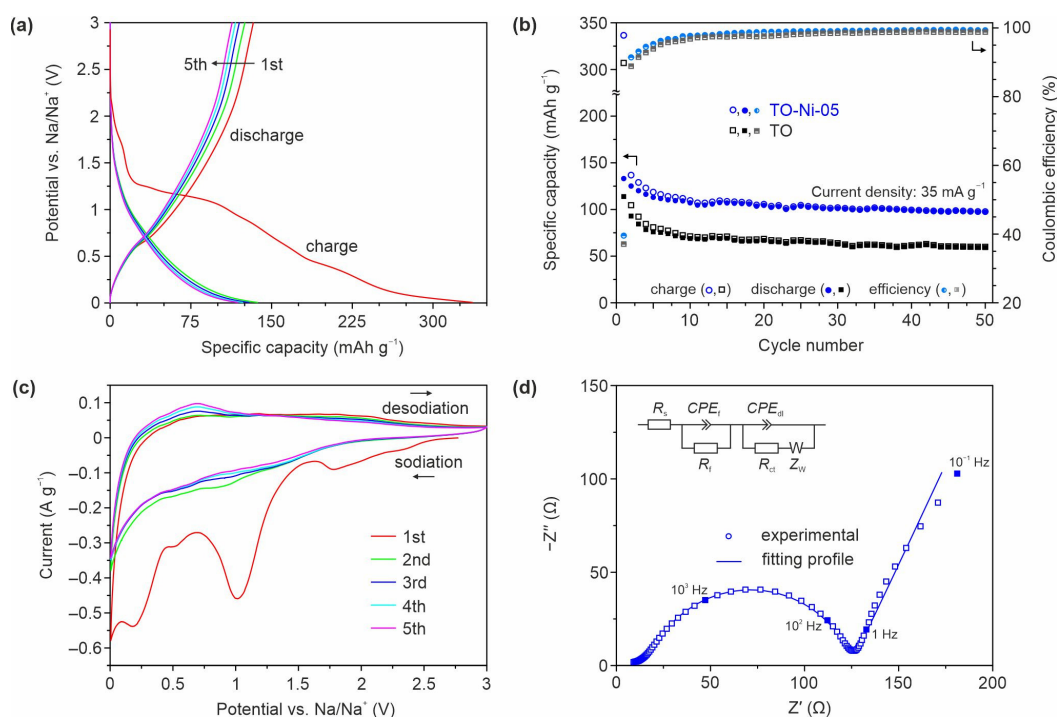


Figure 8. Sodium storage characteristics of analyzed $\text{TiO}_2(\text{B})$ products. The five initial voltage profiles at $35 \text{ mA} \cdot \text{g}^{-1}$ for the TO-Ni-05 material (a) and the corresponding correlation of its specific capacity with cycle number as compared to that for unmodified titanium dioxide (b). CV curves for Ni-doped $\text{TiO}_2(\text{B})$ registered at a scan rate of $0.1 \text{ mV} \cdot \text{s}^{-1}$ (c). Nyquist diagram for TO-Ni-05 electrode after five initial CV cycles and electrical equivalent circuit (inset) used for fitting the experimental data (d).

Figure 8b compares the cycling performance of unmodified and Ni-doped bronze TiO_2 nanobelts. It can be observed that TO-Ni-05 material maintained a capacity of around $97 \text{ mAh} \cdot \text{g}^{-1}$ after 50 cycles with a Coulombic efficiency of $\sim 99.3\%$. This is much higher than the corresponding values of $59 \text{ mAh} \cdot \text{g}^{-1}$ and 98.8% observed for the TO electrode for the same duration of cycling. Retentions of nearly 73% (TO-Ni-05 sample) and 52% (TO product) of the initial desodiation capacity were observed after 50 charge/discharge tests, revealing more stable Na^+ insertion/extraction into/from Ni-modified titanium dioxide.

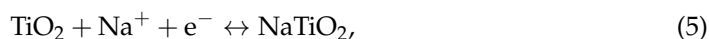
Figure 8c displays the CV curves of the TO-Ni-05 electrode measured in the potential range of $0.005\text{--}3 \text{ V}$ (vs. Na/Na^+). Obviously, the current response during the first cathodic sweep was much higher than that in subsequent scans, confirming the occurrence of irreversible reactions associated with electrolyte reduction (around 1.01 V), decomposition of organics, formation of amorphous phase(s), and trapping of Na^+ ions [71,73]. Furthermore, the intensive peak at the end of the cycle may have involved the sodiation of carbon in the electrode. Regarding the anode side, it should be noted that, from the second CV onward, the broad peak at $0.4\text{--}0.9 \text{ V}$ became pronounced. According to the literature, this may be related to Na^+ extraction from $\text{TiO}_2(\text{B})$ [74]. Upon subsequent cycling, the current of the peak increased, assuming activation of the structure. On the other hand, no distinguishable cathodic feature was detected in the second or subsequent cyclic sweeps. A similar phenomenon was previously observed in a study on nanoparticulate $\text{TiO}_2(\text{B})$ [73]. It was established that Na^+ insertion into bronze titanium dioxide occurs in a wide interval of potentials (mainly below 1 V) [22,27]. Lastly, contrary to recent results [73,75], no characteristic anode peak was registered for conductive carbon desodiation, suggesting its negligible effect on the overall storage capacity of the TO-Ni-05 electrode.

In order to study the relationship among battery performance, kinetic characteristics, and diffusion phenomenon, the EIS spectrum of TO-Ni-05 electrode was recorded at the end (fully desodiated) of the fifth CV cycle (after a 5 h rest). Three main contributions can be observed in the Nyquist plot (Figure 8d): interfacial effects on the SEI layer, mi-

gration of charge carriers through the double layer at the electrode/electrolyte surface, and mass transport within the solid phase, expressed by the deformed semicircle in the high-to-medium-frequency region and low-frequency sloping line. Further analysis of the impedance spectrum was performed using the standard equivalent circuit model, as presented in the inset of Figure 8d. R_s , R_f , CPE_f , R_{ct} , CPE_{dl} , and Z_w in the circuit denote the resistance of the cell (electrolyte, separator, and electrodes), the resistance and capacitance of the interfacial layer, charge transfer resistance, double-layer capacitance, and Warburg impedance. The collected data (Table S3, Supplementary Materials) show that R_{ct} for the TO-Ni-05 sample was equal to approximately 104 Ω , indicating its appropriate electronic and ionic conductivity. To further evaluate the effects of Ni^{2+} ions embedding into the bronze titanium dioxide lattice, the diffusion coefficient of electroactive species D_{Na} ($cm^2 \cdot s^{-1}$) was determined using Equation (4).

$$D_{Na} = \frac{R^2 T^2}{2S^2 n^4 F^4 C_{Na}^2 \sigma_W^2} \quad (4)$$

where R is the gas constant ($8.314 \text{ J} \cdot \text{mol}^{-1} \cdot \text{K}^{-1}$), T is the absolute temperature (298.15 K), S is the geometric area of the electrode (0.5 cm^2), n is the number of electrons transferred during the reaction presented in Equation (5), F is the Faraday constant ($96,500 \text{ C} \cdot \text{mol}^{-1}$), C_{Na} is the concentration of Na^+ species in the material ($17 \times 10^{-3} \text{ mol} \cdot \text{cm}^{-3}$), and σ_W is the Warburg factor, which can be determined from Equation (6) through linear fitting of the Z' vs. $\omega^{-1/2}$ plot (Figure S9, Supplementary Materials).



$$Z' = R_s + R_{ct} + \sigma_W \omega^{-1/2}, \quad (6)$$

where Z' is the real part of the impedance (Ω), and ω is the angular frequency (s^{-1}).

According to the calculations, the chemical diffusion coefficient of sodium ions for the Ni-doped sample was $6.84 \times 10^{-13} \text{ cm}^2 \cdot \text{s}^{-1}$. Using the same methodology (i.e., EIS) of D_{Na} determination, this value is better than that obtained for previously reported TiO_2 materials, including anatase/C nanoparticles ($1.56 \times 10^{-14} \text{ cm}^2 \cdot \text{s}^{-1}$) [76], rutile TiO_2 nanoparticles ($9.9 \times 10^{-15} \text{ cm}^2 \cdot \text{s}^{-1}$) [77], and anatase/C nanofibers ($2.0 \times 10^{-13} \text{ cm}^2 \cdot \text{s}^{-1}$) [78]. Furthermore, the calculated D_{Na} is comparable with that of other modified titanium-based oxides for SIB anodes, as shown in Table S4 (Supplementary Materials). According to the above-mentioned data, it is reasonable to expect that the D_{Na} of bronze titanium dioxide is increased after Ni doping.

4. Conclusions

In summary, herein, a hydrothermal route was applied to synthesize mesoporous belt-like $TiO_2(B)$ nanostructures doped with nickel (Ni/Ti atomic ratios of 0.02, 0.05, and 0.08) and zinc (Zn/Ti = 0.02 and 0.05) with a specific surface area and pore volume reaching $114 \text{ m}^2 \cdot \text{g}^{-1}$ and $0.48 \text{ cm}^3 \cdot \text{g}^{-1}$. According to the analysis of XRD data, nickel doping increased the unit cell volume of bronze titanium dioxide by 4% (Ni/Ti = 0.05), confirming the incorporation of Ni^{2+} ions at the Ti^{4+} positions with the formation of a substitutional solid solution. Indeed, the Ni^{2+} ion is bigger (0.69 \AA) than Ti^{4+} (0.605 \AA), resulting in lattice distortions after substitution. The generation of localized Ni $3d$ defect states within the band gap of $TiO_2(B)$ was confirmed by UV-Vis studies, revealing that the band gap energy was reduced from 3.28 to 2.70 eV after doping. XPS studies revealed an oxygen deficiency for Ni-doped $TiO_2(B)$. According to EPR, F -centers, which may represent the conduction band electrons "trapped" with oxygen vacancies, exist in the nickel-containing material. On the other hand, due to its large ionic radius, zinc (0.74 \AA) hardly entered into $TiO_2(B)$ crystal structure, nevertheless provoking a band gap narrowing effect (to 3.21 eV). The EIS technique revealed that the conductivity of nickel- and zinc-containing titanium dioxide increased to $2.24 \times 10^{-8} \text{ S} \cdot \text{cm}^{-1}$ (Ni/Ti = 0.05) and $3.29 \times 10^{-9} \text{ S} \cdot \text{cm}^{-1}$

(Zn/Ti = 0.02), exceeding that of the undoped sample ($1.05 \times 10^{-10} \text{ S}\cdot\text{cm}^{-1}$). The galvanostatic charge/discharge cycling of materials in lithium cells showed a favorable effect of nickel and zinc doping on the reversibility of the electrochemical process. Among the tested samples, Ni-containing $\text{TiO}_2(\text{B})$ nanobelts with an Ni/Ti atomic ratio of 0.05 demonstrated the best battery performance. In particular, after 100 charge/discharge cycles, a reversible capacity of $173 \text{ mAh}\cdot\text{g}^{-1}$ was achieved for nickel-doped $\text{TiO}_2(\text{B})$ at the current density of $50 \text{ mA}\cdot\text{g}^{-1}$, whereas unmodified and zinc-doped bronze TiO_2 electrodes maintained 140 and $151 \text{ mAh}\cdot\text{g}^{-1}$. Moreover, Ni doping improved the rate performance of $\text{TiO}_2(\text{B})$ nanobelts. Concerning its operation in sodium cells, it was found that nickel-containing material exhibited improved cycling with a specific capacity of about $97 \text{ mAh}\cdot\text{g}^{-1}$ after 50 cycles at the current load of $35 \text{ mA}\cdot\text{g}^{-1}$. EIS studies identified a D_{Na} of $6.84 \times 10^{-13} \text{ cm}^2\cdot\text{s}^{-1}$ for Ni-doped $\text{TiO}_2(\text{B})$ (Ni/Ti = 0.05). The main factors determining the enhanced electrochemical performance of doped $\text{TiO}_2(\text{B})$ were (i) increased electronic conductivity, (ii) improved stability of crystal lattice toward guest ion insertion/extraction, and (iii) facilitated transport of Li^+ and Na^+ . Thus, the current study demonstrates that proper doping might be an effective way to adopt bronze titanium dioxide's properties for its usage in the area of metal-ion batteries.

Supplementary Materials: The following are available online at <https://www.mdpi.com/article/10.3390/nano11071703/s1>: Figure S1. Rietveld plots for unmodified, Ni-doped, and Zn-doped $\text{TiO}_2(\text{B})$ samples (experimental, calculated and difference curves; the vertical bars correspond to the positions of the Bragg reflections); Figure S2. EDX spectrum (a) and maps of elements (b) for TO-Ni-05 material; Figure S3. N_2 adsorption–desorption isotherms, cumulative pore volume curve, and pore size distribution (inset) for the TO sample; Figure S4. Nyquist diagrams (full-scale view) for the pellets from undoped, Ni-doped, and Zn-modified $\text{TiO}_2(\text{B})$ powders; Figure S5. UV–Vis absorption spectra for TO, TO-Ni-02, and TO-Ni-05 materials in the wavelength range of 550–800 nm; Figure S6. EPR spectra of undoped bronze TiO_2 nanobelts (TO sample); Figure S7. Color of unmodified (a), Ni-doped (b), and Zn-doped (c) $\text{TiO}_2(\text{B})$ samples; Figure S8. Comparison of the rate capability for different $\text{TiO}_2(\text{B})$ nanostructures; Figure S9. Relationship between Z' and $\omega^{-1/2}$ in low-frequency region for TO-Ni-05 employed as SIB anode; Table S1. Rietveld refinement results from XRD data of the undoped, Ni-doped, and Zn-doped $\text{TiO}_2(\text{B})$ samples; Table S2. Surface area of materials shown in Figure S6 and features of their fabrication and testing as LIB electrodes; Table S3. Measured EIS parameters for TO-Ni-05 electrode in sodium half-cell; Table S4. The chemical diffusion coefficient of sodium ions for different Ti-based oxide materials for SIBs anodes.

Author Contributions: D.P.O., S.V.G., and S.L.S. designed the study, carried out the material laboratory work, interpreted the SEM/STEM, EDX, XRD, UV–Vis, and battery performance data, participated in data analysis, and drafted the manuscript; A.V.G. calculated the structural parameters through the Rietveld method; A.M.Z. performed and explained the EPR measurements; D.P.O. and A.A.S. synthesized the materials, carried out the electrochemical investigations, and interpreted data; A.B.P. measured and interpreted the electroconductive properties of materials; A.Y.U. collected and analyzed XPS data; V.G.K. carried out the microstructure characterization and elemental analysis; V.Y.M. studied the textural characteristics of materials; I.A.T. investigated the magnetic properties of samples; V.I.S. coordinated the study and helped draft the manuscript. All authors read and agreed to the published version of the manuscript.

Funding: This work was supported by funding from the Russian Science Foundation (grant No. 19-73-10017).

Institutional Review Board Statement: Not applicable.

Informed Consent Statement: Not applicable.

Data Availability Statement: The data presented in this study are available on request from the corresponding author.

Acknowledgments: For technical guidance of experiments, the authors are grateful to Sc.D. V.V. Zhelezov (Institute of Chemistry FEB RAS). D.P. Opra acknowledges the Government of Primorsky Krai (Far Eastern Federal District, Russian Federation) for the award to researchers of scientific organizations geographically located in the Primorye territory (Order No. 23a-1140 from 2 November 2020).

Conflicts of Interest: The authors declare no conflict of interest.

References

1. Fehse, M.; Ventosa, E. Is TiO₂(B) the future of titanium-based battery materials? *Chempluschem* **2015**, *80*, 785–795. [[CrossRef](#)]
2. Münster, P.; Diehl, M.; Frerichs, J.E.; Börner, M.; Hansen, M.R.; Winter, M.; Niehoff, P. Effect of Li plating during formation of lithium ion batteries on their cycling performance and thermal safety. *J. Power Sources* **2021**, *484*, 229306. [[CrossRef](#)]
3. Ivanishchev, A.V.; Ivanishcheva, I.A. Ion transport in lithium electrochemical systems: Problems and solutions. *Rus. J. Electrochem.* **2020**, *56*, 907–928. [[CrossRef](#)]
4. Ushakov, A.V.; Makhov, S.V.; Gridina, N.A.; Ivanishchev, A.V.; Gamayunova, I.M. Rechargeable lithium-ion system based on lithium-vanadium(III) phosphate and lithium titanate and the peculiarity of it functioning. *Mon. Chem. Chem. Mon.* **2019**, *150*, 499–509. [[CrossRef](#)]
5. Sterina, I.A.; Shaydullin, R.R.; Desyatov, A.V.; Kulova, T.L.; Yaroslavtsev, A.B. Effect of carbon and N-doped carbon nanomaterials on the electrochemical performance of lithium titanate-based composites. *Electrochim. Acta* **2020**, *364*, 137330. [[CrossRef](#)]
6. Yan, X.; Wang, Z.; He, M.; Hou, Z.; Xia, T.; Liu, G.; Chen, X. TiO₂ nanomaterials as anode materials for lithium-ion rechargeable batteries. *Energy Technol.* **2015**, *3*, 801–814. [[CrossRef](#)]
7. Zhang, W.; Zhang, Y.; Yu, L.; Wu, N.-L.; Huang, H.; Wei, M. TiO₂-B nanowires via topological conversion with enhanced lithium-ion intercalation properties. *J. Mater. Chem. A* **2019**, *7*, 3842–3847. [[CrossRef](#)]
8. Vazquez-Santos, M.B.; Tartaj, P.; Morales, E.; Amarilla, J.M. TiO₂ nanostructures as anode materials for Li/Na-ion batteries. *Chem. Rec.* **2018**, *18*, 1178–1191. [[CrossRef](#)] [[PubMed](#)]
9. Panduwinata, D.; Gale, J.D. A first principles investigation of lithium intercalation in TiO₂-B. *J. Mater. Chem.* **2009**, *19*, 3931. [[CrossRef](#)]
10. Okumura, T.; Fukutsuka, T.; Yanagihara, A.; Orikasa, Y.; Arai, H.; Ogumi, Z.; Uchimoto, Y. Electronic and local structural changes with lithium-ion insertion in TiO₂-B: X-ray absorption spectroscopy study. *J. Mater. Chem.* **2011**, *21*, 15369–15377. [[CrossRef](#)]
11. Zukalová, M.; Kalbáč, M.; Kavan, L.; Exnar, I.; Graetzel, M.; Kalbáč, M.; Kavan, L.; Exnar, I.; Graetzel, M. Pseudocapacitive lithium storage in TiO₂(B). *Chem. Mater.* **2005**, *17*, 1248–1255. [[CrossRef](#)]
12. Hasa, I.; Mariyappan, S.; Saurel, D.; Adelhelm, P.; Kuposov, A.Y.; Masquelier, C.; Croguennec, L.; Casas-Cabanas, M. Challenges of today for Na-based batteries of the future: From materials to cell metrics. *J. Power Sources* **2021**, *482*, 228872. [[CrossRef](#)]
13. Skundin, A.M.; Kulova, T.L.; Yaroslavtsev, A.B. Sodium-ion batteries (a review). *Rus. J. Electrochem.* **2018**, *54*, 113–152. [[CrossRef](#)]
14. Hou, H.; Qiu, X.; Wei, W.; Zhang, Y.; Ji, X. Carbon anode materials for advanced sodium-ion batteries. *Adv. Energy Mater.* **2017**, *7*, 1602898. [[CrossRef](#)]
15. Górká, J.; Vix-Guterl, C.; Matei Ghimbeu, C. Recent progress in design of biomass-derived hard carbons for sodium ion batteries. *C J. Carbon Res.* **2016**, *2*, 24. [[CrossRef](#)]
16. Wang, Y.; Zhu, W.; Guerfi, A.; Kim, C.; Zaghbi, K. Roles of Ti in electrode materials for sodium-ion batteries. *Front. Energy Res.* **2019**, *7*. [[CrossRef](#)]
17. Wang, W.; Liu, Y.; Wu, X.; Wang, J.; Fu, L.; Zhu, Y.; Wu, Y.; Liu, X. Advances of TiO₂ as negative electrode materials for sodium-ion batteries. *Adv. Mater. Technol.* **2018**, *3*, 1800004. [[CrossRef](#)]
18. Dawson, J.A.; Robertson, J. Improved calculation of Li and Na intercalation properties in anatase, rutile, and TiO₂(B). *J. Phys. Chem. C* **2016**, *120*, 22910–22917. [[CrossRef](#)]
19. Liu, Y.; Zhao, F.; Li, J.; Li, Y.; McLeod, J.A.; Liu, L. Influence of crystal phase on TiO₂ nanowire anodes in sodium ion batteries. *J. Mater. Chem. A* **2017**, *5*, 20005–20013. [[CrossRef](#)]
20. Kang, S.H.; Jo, Y.N.; Prasanna, K.; Santhoshkumar, P.; Joe, Y.C.; Vediappan, K.; Gnanamuthu, R.; Lee, C.W. Bandgap tuned and oxygen vacant TiO_{2-x} anode materials with enhanced electrochemical properties for lithium ion batteries. *J. Ind. Eng. Chem.* **2019**, *71*, 177–183. [[CrossRef](#)]
21. Xie, F.; Zhu, J.; Li, Y.; Shen, D.; Abate, A.; Wei, M. TiO₂-B as an electron transporting material for highly efficient perovskite solar cells. *J. Power Sources* **2019**, *415*, 8–14. [[CrossRef](#)]
22. Huang, J.P.; Yuan, D.D.; Zhang, H.Z.; Cao, Y.L.; Li, G.R.; Yang, H.X.; Gao, X.P. Electrochemical sodium storage of TiO₂(B) nanotubes for sodium ion batteries. *RSC Adv.* **2013**, *3*, 12593. [[CrossRef](#)]
23. Agostini, M.; Brutti, S.; Navarra, M.A.; Panero, S.; Reale, P.; Matic, A.; Scrosati, B. A high-power and fast charging Li-ion battery with outstanding cycle-life. *Sci. Rep.* **2017**, *7*, 1104. [[CrossRef](#)] [[PubMed](#)]
24. Giannuzzi, R.; Manca, M.; De Marco, L.; Belviso, M.R.; Cannavale, A.; Sibillano, T.; Giannini, C.; Cozzoli, P.D.; Gigli, G. Ultrathin TiO₂(B) nanorods with superior lithium-ion storage performance. *ACS Appl. Mater. Interfaces* **2014**, *6*, 1933–1943. [[CrossRef](#)]
25. Mason, C.W.; Yeo, I.; Saravanan, K.; Balaya, P. Interconnected nanofibrous titanium dioxide bronze: An emerging lithium ion anode material for high rate performance. *RSC Adv.* **2013**, *3*, 2935. [[CrossRef](#)]
26. Pineda-Aguilar, N.; Garza-Tovar, L.L.; Sánchez-Cervantes, E.M.; Sánchez-Domínguez, M. Preparation of TiO₂(B) by microemulsion mediated hydrothermal method: Effect of the precursor and its electrochemical performance. *J. Mater. Sci. Mater. Electron.* **2018**, *29*, 15464–15479. [[CrossRef](#)]
27. Lee, J.; Lee, J.K.; Chung, K.Y.; Jung, H.-G.; Kim, H.; Mun, J.; Choi, W. Electrochemical investigations on TiO₂-B nanowires as a promising high capacity anode for sodium-ion batteries. *Electrochim. Acta* **2016**, *200*, 21–28. [[CrossRef](#)]

28. Meng, Y.; Wang, D.; Wei, Y.; Zhu, K.; Zhao, Y.; Bian, X.; Du, F.; Liu, B.; Gao, Y.; Chen, G. Competition between insertion of Li^+ and Mg^{2+} : An example of TiO_2 -B nanowires for Mg rechargeable batteries and $\text{Li}^+/\text{Mg}^{2+}$ hybrid-ion batteries. *J. Power Sources* **2017**, *346*, 134–142. [[CrossRef](#)]
29. Liu, Y.; Chen, W.; Yang, C.; Wei, Q.; Wei, M. Hierarchical TiO_2 -B composed of nanosheets with exposed {010} facets as a high-performance anode for lithium ion batteries. *J. Power Sources* **2018**, *392*, 226–231. [[CrossRef](#)]
30. Wang, Y.; Chen, T.; Mu, Q. Electrochemical performance of W-doped anatase TiO_2 nanoparticles as an electrode material for lithium-ion batteries. *J. Mater. Chem.* **2011**, *21*, 6006. [[CrossRef](#)]
31. Zhang, W.; Gong, Y.; Mellott, N.P.; Liu, D.; Li, J. Synthesis of nickel doped anatase titanate as high performance anode materials for lithium ion batteries. *J. Power Sources* **2015**, *276*, 39–45. [[CrossRef](#)]
32. Anh, L.T.; Rai, A.K.; Thi, T.V.; Gim, J.; Kim, S.; Shin, E.-C.; Lee, J.-S.; Kim, J. Improving the electrochemical performance of anatase titanium dioxide by vanadium doping as an anode material for lithium-ion batteries. *J. Power Sources* **2013**, *243*, 891–898. [[CrossRef](#)]
33. Feng, Y.; Liu, H.; Liu, Y.; Zhao, F.; Li, J.; He, X. Defective TiO_2 -graphene heterostructures enabling in-situ electrocatalyst evolution for lithium-sulfur batteries. *J. Energy Chem.* **2021**, *62*, 508–515. [[CrossRef](#)]
34. Kyeremateng, N.A.; Vacandio, F.; Sougrati, M.-T.; Martinez, H.; Jumas, J.-C.; Knauth, P.; Djenizian, T. Effect of Sn-doping on the electrochemical behaviour of TiO_2 nanotubes as potential negative electrode materials for 3D Li-ion micro batteries. *J. Power Sources* **2013**, *224*, 269–277. [[CrossRef](#)]
35. Gnedenkov, S.V.; Sinebryukhov, S.L.; Zheleznov, V.V.; Opra, D.P.; Voit, E.I.; Modin, E.B.; Sokolov, A.A.; Ustinov, A.Y.; Sergienko, V.I. Effect of Hf-doping on electrochemical performance of anatase TiO_2 as an anode material for lithium storage. *R. Soc. Open Sci.* **2018**, *5*, 171811. [[CrossRef](#)]
36. Zhang, Y.; Ding, Z.; Foster, C.W.; Banks, C.E.; Qiu, X.; Ji, X. Oxygen vacancies evoked blue $\text{TiO}_2(\text{B})$ nanobelts with efficiency enhancement in sodium storage behaviors. *Adv. Funct. Mater.* **2017**, *27*, 1700856. [[CrossRef](#)]
37. Lei, Y.; Li, J.; Wang, Z.; Sun, J.; Chen, F.; Liu, H.; Ma, X.; Liu, Z. Atomic-scale investigation of a new phase transformation process in TiO_2 nanofibers. *Nanoscale* **2017**, *9*, 4601–4609. [[CrossRef](#)]
38. Shannon, R.D. Revised effective ionic radii and systematic studies of interatomic distances in halides and chalcogenides. *Acta Crystallogr. Sect. A* **1976**, *32*, 751–767. [[CrossRef](#)]
39. Ni, J.; Fu, S.; Wu, C.; Zhao, Y.; Maier, J.; Yu, Y.; Li, L. Superior sodium storage in $\text{Na}_2\text{Ti}_3\text{O}_7$ nanotube arrays through surface engineering. *Adv. Energy Mater.* **2016**, *6*, 1502568. [[CrossRef](#)]
40. Ganesh, I.; Gupta, A.K.; Kumar, P.P.; Sekhar, P.S.C.; Radha, K.; Padmanabham, G.; Sundararajan, G. Preparation and characterization of Ni-doped materials for photocurrent and photocatalytic applications. *Sci. World J.* **2012**, *2012*, 127326. [[CrossRef](#)] [[PubMed](#)]
41. She, H.; Zhou, H.; Li, L.; Wang, L.; Huang, J.; Wang, Q. Nickel-doped excess oxygen defect titanium dioxide for efficient selective photocatalytic oxidation of benzyl alcohol. *ACS Sustain. Chem. Eng.* **2018**, *6*, 11939–11948. [[CrossRef](#)]
42. Arif Sher Shah, M.S.; Zhang, K.; Park, A.R.; Kim, K.S.; Park, N.-G.; Park, J.H.; Yoo, P.J. Single-step solvothermal synthesis of mesoporous Ag- TiO_2 -reduced graphene oxide ternary composites with enhanced photocatalytic activity. *Nanoscale* **2013**, *5*, 5093. [[CrossRef](#)]
43. Bakhmutov, V.I. Strategies for solid-state NMR studies of materials: From diamagnetic to paramagnetic porous solids. *Chem. Rev.* **2011**, *111*, 530–562. [[CrossRef](#)] [[PubMed](#)]
44. Tian, J.; Gao, H.; Kong, H.; Yang, P.; Zhang, W.; Chu, J. Influence of transition metal doping on the structural, optical, and magnetic properties of TiO_2 films deposited on Si substrates by a sol-gel process. *Nanoscale Res. Lett.* **2013**, *8*, 533. [[CrossRef](#)] [[PubMed](#)]
45. Bashir, A.; Bashir, F.; Sultan, M.; Mubeen, M.; Iqbal, A.; Akhter, Z. Influence of nickel and lanthanum ions co-doping on photocatalytic properties of TiO_2 for effective degradation of reactive yellow 145 in the visible region. *J. Sol. Gel Sci. Technol.* **2020**, *93*, 438–451. [[CrossRef](#)]
46. Biju, V.; Abdul Khadar, M. DC conductivity of consolidated nanoparticles of NiO. *Mater. Res. Bull.* **2001**, *36*, 21–33. [[CrossRef](#)]
47. Wang, Y.; Zhang, R.; Li, J.; Li, L.; Lin, S. First-principles study on transition metal-doped anatase TiO_2 . *Nanoscale Res. Lett.* **2014**, *9*, 46. [[CrossRef](#)]
48. Smirnova, N.; Petrik, I.; Vorobets, V.; Kolbasov, G.; Eremenko, A. Sol-gel synthesis, photo- and electrocatalytic properties of mesoporous TiO_2 modified with transition metal ions. *Nanoscale Res. Lett.* **2017**, *12*, 239. [[CrossRef](#)] [[PubMed](#)]
49. Brodbeck, C.M.; Bukrey, R.R. Model calculations for the coordination of Fe^{3+} and Mn^{2+} ions in oxide glasses. *Phys. Rev. B* **1981**, *24*, 2334–2342. [[CrossRef](#)]
50. Martos, M.; Julián, B.; Dehouli, H.; Gourier, D.; Cordoncillo, E.; Escribano, P. Synthesis and characterization of $\text{Ti}_{1-2x}\text{Nb}_x\text{Ni}_x\text{O}_{2-x/2}$ solid solutions. *J. Solid State Chem.* **2007**, *180*, 679–687. [[CrossRef](#)]
51. Weil, J.; Bolton, J.R. *Electron Paramagnetic Resonance: Elementary Theory and Practical Applications*; Wiley-Interscience: Hoboken, NJ, USA, 2007; ISBN 9780471754961.
52. Rane, K.S.; Mhalsiker, R.; Yin, S.; Sato, T.; Cho, K.; Dunbar, E.; Biswas, P. Visible light-sensitive yellow $\text{TiO}_{2-x}\text{N}_x$ and Fe-N co-doped $\text{Ti}_{1-y}\text{Fe}_y\text{O}_{2-x}\text{N}_x$ anatase photocatalysts. *J. Solid State Chem.* **2006**, *179*, 3033–3044. [[CrossRef](#)]
53. Ran, Y.; Seung-li, S.; Han, J.; Joo, K.; Sung, C. Ferromagnetic properties of Ni-doped rutile $\text{TiO}_{2-\delta}$. *J. Korean Phys. Soc.* **2007**, *50*, 638. [[CrossRef](#)]

54. Coey, J.M.D.; Venkatesan, M.; Fitzgerald, C.B. Donor impurity band exchange in dilute ferromagnetic oxides. *Nat. Mater.* **2005**, *4*, 173–179. [[CrossRef](#)] [[PubMed](#)]
55. Wang, Q.; Liu, X.; Wei, X.; Dai, J.; Li, W. Ferromagnetic property of Co and Ni doped TiO₂ nanoparticles. *J. Nanomater.* **2015**, *2015*, 1–5. [[CrossRef](#)]
56. Dakhel, A.A.; Hamad, H.; Jaafar, A. Investigation to the structural, optical, and magnetic properties of synthesized Ni-doped anatase nanoparticles: Essential role of treatment in hydrogen on long-range ferromagnetic order. *J. Supercond. Nov. Magn.* **2019**, *32*, 253–260. [[CrossRef](#)]
57. Beuvier, T.; Richard-Plouet, M.; Mancini-Le Granvalet, M.; Brousse, T.; Crosnier, O.; Brohan, L. TiO₂(B) nanoribbons as negative electrode material for lithium ion batteries with high rate performance. *Inorg. Chem.* **2010**, *49*, 8457–8464. [[CrossRef](#)]
58. Dylla, A.G.; Henkelman, G.; Stevenson, K.J. Lithium insertion in nanostructured TiO₂(B) architectures. *Acc. Chem. Res.* **2013**, *46*, 1104–1112. [[CrossRef](#)] [[PubMed](#)]
59. Song, M.-S.; Kim, R.-H.; Baek, S.-W.; Lee, K.-S.; Park, K.; Benayad, A. Is Li₄Ti₅O₁₂ a solid-electrolyte-interphase-free electrode material in Li-ion batteries? Reactivity between the Li₄Ti₅O₁₂ electrode and electrolyte. *J. Mater. Chem. A* **2014**, *2*, 631–636. [[CrossRef](#)]
60. Brutti, S.; Gentili, V.; Reale, P.; Carbone, L.; Panero, S. Mitigation of the irreversible capacity and electrolyte decomposition in a LiNi_{0.5}Mn_{1.5}O₄/nano-TiO₂ Li-ion battery. *J. Power Sources* **2011**, *196*, 9792–9799. [[CrossRef](#)]
61. Brutti, S.; Gentili, V.; Menard, H.; Scrosati, B.; Bruce, P.G. TiO₂(B) nanotubes as anodes for lithium batteries: Origin and mitigation of irreversible capacity. *Adv. Energy Mater.* **2012**, *2*, 322–327. [[CrossRef](#)]
62. Wang, Y.; Ren, Y.; Dai, X.; Yan, X.; Huang, B.; Li, J. Electrochemical performance of ZnO-coated Li₄Ti₅O₁₂ composite electrodes for lithium-ion batteries with the voltage ranging from 3 to 0.01 V. *R. Soc. Open Sci.* **2018**, *5*, 180762. [[CrossRef](#)]
63. Huang, H.; Fang, J.; Xia, Y.; Tao, X.; Gan, Y.; Du, J.; Zhu, W.; Zhang, W. Construction of sheet–belt hybrid nanostructures from one-dimensional mesoporous TiO₂(B) nanobelts and graphene sheets for advanced lithium-ion batteries. *J. Mater. Chem. A* **2013**, *1*, 2495. [[CrossRef](#)]
64. Chen, C.; Hu, X.; Zhang, B.; Miao, L.; Huang, Y. Architectural design and phase engineering of N/B-codoped TiO₂(B)/anatase nanotube assemblies for high-rate and long-life lithium storage. *J. Mater. Chem. A* **2015**, *3*, 22591–22598. [[CrossRef](#)]
65. Etacheri, V.; Kuo, Y.; Van der Ven, A.; Bartlett, B.M. Mesoporous TiO₂-B microflowers composed of (110) facet-exposed nanosheets for fast reversible lithium-ion storage. *J. Mater. Chem. A* **2013**, *1*, 12028. [[CrossRef](#)]
66. Wang, J.-F.; Zhang, J.-J.; He, D.-N. Flower-like TiO₂-B particles wrapped by graphene with different contents as an anode material for lithium-ion batteries. *Nano Struct. Nano Objects* **2018**, *15*, 216–223. [[CrossRef](#)]
67. Yan, X.; Zhang, Y.; Zhu, K.; Gao, Y.; Zhang, D.; Chen, G.; Wang, C.; Wei, Y. Enhanced electrochemical properties of TiO₂(B) nanoribbons using the styrene butadiene rubber and sodium carboxyl methyl cellulose water binder. *J. Power Sources* **2014**, *246*, 95–102. [[CrossRef](#)]
68. Shin, K.; Kim, H.J.; Choi, J.-M.; Choi, Y.-M.; Song, M.S.; Park, J.H. Controlled synthesis of skein shaped TiO₂-B nanotube cluster particles with outstanding rate capability. *Chem. Commun.* **2013**, *49*, 2326. [[CrossRef](#)] [[PubMed](#)]
69. Wessel, C.; Zhao, L.; Urban, S.; Ostermann, R.; Djerdj, I.; Smarsly, B.M.; Chen, L.; Hu, Y.-S.; Sallard, S. Ionic-liquid synthesis route of TiO₂(B) nanoparticles for functionalized materials. *Chem. A Eur. J.* **2011**, *17*, 775–779. [[CrossRef](#)]
70. Yang, Y.; Liao, S.; Shi, W.; Wu, Y.; Zhang, R.; Leng, S. Nitrogen-doped TiO₂(B) nanorods as high-performance anode materials for rechargeable sodium-ion batteries. *RSC Adv.* **2017**, *7*, 10885–10890. [[CrossRef](#)]
71. Yan, D.; Pan, L. A new sodium storage mechanism of TiO₂ for sodium ion batteries. *Inorg. Chem. Front.* **2016**, *3*, 464–468. [[CrossRef](#)]
72. Xu, Y.; Zhou, M.; Wen, L.; Wang, C.; Zhao, H.; Mi, Y.; Liang, L.; Fu, Q.; Wu, M.; Lei, Y. Highly ordered three-dimensional Ni-TiO₂ nanoarrays as sodium ion battery anodes. *Chem. Mater.* **2015**, *27*, 4274–4280. [[CrossRef](#)]
73. Wu, L.; Bresser, D.; Buchholz, D.; Passerini, S. Nanocrystalline TiO₂(B) as anode material for sodium-ion batteries. *J. Electrochem. Soc.* **2015**, *162*, A3052–A3058. [[CrossRef](#)]
74. Wang, B.; Zhao, F.; Du, G.; Porter, S.; Liu, Y.; Zhang, P.; Cheng, Z.; Liu, H.K.; Huang, Z. Boron-doped anatase TiO₂ as a high-performance anode material for sodium-ion batteries. *ACS Appl. Mater. Interfaces* **2016**, *8*, 16009–16015. [[CrossRef](#)]
75. Yang, Y.; Ji, X.; Jing, M.; Hou, H.; Zhu, Y.; Fang, L.; Yang, X.; Chen, Q.; Banks, C.E. Carbon dots supported upon N-doped TiO₂ nanorods applied into sodium and lithium ion batteries. *J. Mater. Chem. A* **2015**, *3*, 5648–5655. [[CrossRef](#)]
76. Li, Y.-N.; Su, J.; Lv, X.-Y.; Long, Y.-F.; Yu, H.; Huang, R.-R.; Xie, Y.-C.; Wen, Y.-X. Zn²⁺ doped TiO₂/C with enhanced sodium-ion storage properties. *Ceram. Int.* **2017**, *43*, 10326–10332. [[CrossRef](#)]
77. He, H.; Wang, H.; Sun, D.; Shao, M.; Huang, X.; Tang, Y. N-doped rutile TiO₂/C with significantly enhanced Na storage capacity for Na-ion batteries. *Electrochim. Acta* **2017**, *236*, 43–52. [[CrossRef](#)]
78. Nie, S.; Liu, L.; Liu, J.; Xie, J.; Zhang, Y.; Xia, J.; Yan, H.; Yuan, Y.; Wang, X. Nitrogen-doped TiO₂-C composite nanofibers with high-capacity and long-cycle life as anode materials for sodium-ion batteries. *Nano Micro Lett.* **2018**, *10*, 71. [[CrossRef](#)] [[PubMed](#)]